IX. PLASMA MAGNETOHYDRODYNAMICS AND ENERGY CONVERSION*

Prof. G. A. Brown
Prof. E. N. Carabateas
Prof. R. S. Cooper
Prof. W. H. Heiser
Prof. M. A. Hoffman
Prof. W. D. Jackson
Prof. J. L. Kerrebrock
Prof. J. E. McCune
Prof. J. P. Penhune
Prof. A. H. Shapiro
Prof. R. E. Stickney
M. T. Badrawi
A. N. Chandra
J. L. Coggins
R. Dethlefsen
D. A. East
R. K. Edwards
J. R. Ellis, Jr.
J. W. Gadzuk
W. J. Hastings
J. B. Heywood
G. B. Kliman
A. G. F. Kniazzeh
M. F. Koskinen
K. S. Lee
D. Y-S. Lou
B. T. Lubin
M. A. Lutz
C. A. McNary
E. S. Pierson
R. P. Porter
A. Shavit
A. Solbes
P. B-S. Sun
R. J. Thome
W. F. Ulvang
J. C. Wissmiller
G. W. Zeiders, Jr.

A. CONSTANT-PRESSURE, LIQUID-METAL, MHD CONDUCTION GENERATOR

1. Introduction

One of the drawbacks of the constant-area liquid-metal conduction generator is the high-pressure drop associated with its operation. The large increase in pressure drop over that which would occur under ordinary hydrodynamic conditions is due to large $\overline{J} \times \overline{B}$ body forces induced by the magnetic field and to increased frictional pressure drop caused by the flattening of the velocity profile by the magnetic field. The effects of these $\overline{J} \times \overline{B}$ forces cannot be alleviated simply by making the generator physically larger, which is possible with friction forces, since the former are body forces while the latter are surface forces.

A possible solution is to construct the generator with a diverging channel and thus convert (or partially convert) the dynamic head at the generator inlet to static pressure; this would offset the large forces mentioned above. The features and limitations of this approach are considered in this report.

2. Available Dynamic Head

The total or stagnation pressure at the generator inlet is given by the sum of the static pressure and the dynamic head, $1/2\ \rho v^2$, at that point. The maximum increase in static pressure is obtained from a complete deceleration of the flow to zero velocity, and represents an upper limit on the increase in static pressure obtainable by diverging the generator channel.

For example, for a liquid metal with density, ρ, equal to 1000 kgm/m^3, and an inlet velocity of 40 m/sec (which is quite high for a liquid-flow system) the upper limit is

*This work was supported in part by the U.S. Air Force (Aeronautical Systems Division) under Contract AF33(615)-1083 with the Air Force Aero Propulsion Laboratory, Wright-Patterson Air Force Base, Ohio; and in part by the National Science Foundation (Grant GK-19).

$$1/2\ \rho v^2 = 8 \times 10^5 \frac{\text{ntn}}{\text{m}^2}.$$

[Note: $\rho_{NaK} \approx 850$ kgm/m^3; the density of Hg is of the order of 10^4 kgm/m^3. The overall effect on dynamic head would not be greater than in this example, since the velocities attainable in an Hg system would be much lower than the velocity used here.]

This amounts to approximately 8 atmospheres, or approximately 120 psi, which is negligible compared with the pressure drop of several thousand psi which would be required by a generator in the megawatt range.

3. Fluid Mechanical Effects

The complete deceleration of the fluid to zero velocity that is assumed implies an infinite channel divergence or simply a free jet flowing into a reservoir. Since the generator cannot physically be located in the infinitesimal length between the jet entrance to the reservoir and the reservoir and the velocity leaving the generator must actually have a finite value, the divergence must be limited and the static pressure recovery is then somewhat less than that determined. Moreover, the amount of allowable channel divergence under actual conditions must be considered.

In ordinary hydrodynamic flow through a diverging channel, a backflow occurs along the walls if the divergence is too great. This is the result of the inability of the slowly moving fluid near the channel walls (which has correspondingly less momentum than the fluid in the core of the flow) to oppose the adverse pressure gradient arising from the channel divergence. Similar effects may govern the amount of allowable channel divergence in the presence of a magnetic field. Indeed, if the divergence is too great, the field may actually freeze the fluid near the channel walls with the result that there is a constant cross-section flow down the center of the diverging channel.

4. Simplified Analysis

Consider the steady-state, frictionless flow of an incompressible fluid with scalar conductivity, σ, through a channel with the geometry and coordinates given in Fig. IX-1.

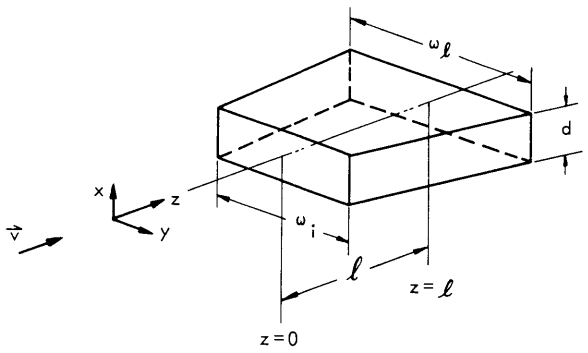

Fig. IX-1. Variable-area MHD generator duct.

The channel has constant depth d, length ℓ, initial width ω_i, final width ω_ℓ, and continuous electrodes. It is assumed that the velocity $\vec{v} = v(z)\,\vec{i}_z$ is uniform over any cross section, the magnetic field $\vec{B} = \vec{B}_i i_x$ is constant, and the inlet conditions are specified. From the geometry of the channel,

$$A(z) = \frac{d}{\ell}[z\omega_\ell + (\ell - z)\omega_i], \tag{1}$$

where the subscript i denotes inlet quantities.

From the continuity equation,

$$v(z) = \frac{v_i \ell}{\left[\ell + z\left(\frac{\omega_\ell}{\omega_i} - 1\right)\right]}. \tag{2}$$

A loading factor may be defined as $k = -\frac{E}{vB} = \frac{V}{vB\omega}$, where $E = -\frac{V}{\omega}$. Then

$$\left.\begin{aligned} E &= -kvB \\ J &= \sigma(1-k)\,vB \end{aligned}\right\}. \tag{3}$$

Substitution of (1-3) in the momentum equation and integrating yields

$$p_o - p_i = -\frac{\rho v_i^2}{2}\left[\left(\frac{\omega_i}{\omega_\ell}\right)^2 - 1\right] - \frac{\sigma(1-k)\,B_i^2 v_i \ell}{\left(\frac{\omega_\ell}{\omega_i} - 1\right)} \ln\frac{\omega_\ell}{\omega_i}. \tag{4}$$

To obtain the condition for a device with no pressure drop, set the left side of (4) equal to zero. Then the inlet velocity required in terms of the fluid properties and the channel geometry is given by

$$v_i = \frac{2\sigma(1-k)\,B_i^2 \ell \ln\frac{\omega_\ell}{\omega_i}}{\rho\left[1 - \left(\frac{\omega_i}{\omega_\ell}\right)^2\right]\left(\frac{\omega_\ell}{\omega_i} - 1\right)}. \tag{5}$$

Consider an experimental generator in which the channel geometry and fluid properties, field strength, and loading conditions are specified. A generator suitable for an experimental test facility would have the following dimensions:

$d = 5$ cm $= 0.05$ m
$\ell = 30$ cm $= 0.3$ m
$\omega_i = 18$ cm $= 0.18$ m
$\omega_\ell = 24$ cm $= 0.24$ m.

The dimensions chosen result in an included angle of divergence of 11.5°. This is a reasonable estimate for an upper limit on the divergence angle before the separation or possible freezing effects occur.

If the magnetic-field strength, B_i, is chosen to be $2w/m^2$, and the loading factor is 0.5, substitution of these values, together with the fluid properties for NaK and Hg, leads to the required inlet velocities to restrict the pressure drop to zero.

NaK: v_i = 6800 m/sec

Hg: v_i = 184 m/sec.

Note that the NaK inlet velocity corresponds to a fluid flow greater than Mach 4.

If the flow rate is now set at a typical value in a test facility, 250 gpm, the corresponding inlet velocity can be obtained. This calculation results in an inlet velocity of 1.76 m/sec for the geometry selected. Substitution of this velocity in the original pressure-drop equation gives the required values for the pressure drop under these conditions. Table IX-1 summarizes the results obtained for NaK and Hg under various conditions of magnetic-field strength.

Table IX-1. Comparison of results attainable with NaK and Hg.

$B_i \frac{w}{m^2}$	Δp(psi)		P_{out}(kw)		V	I(amps × 10^3)	
	NaK	Hg	NaK	Hg	(volts)	NaK	Hg
2	326	140	17.6	7.61	0.316	55.6	24.1
1.5	184	78	9.9	4.28	0.237	41.8	18.1
1	81.7	33.8	4.4	1.9	0.158	27.8	12.05

Tabulated quantities other than pressure drop were calculated from the following equations.

$$I = \int_0^1 dJdz = \frac{\sigma(1-k)\, B_i dv_i \ell}{\left(\frac{\omega_\ell}{\omega_i} - 1\right)} \ln \frac{\omega_\ell}{\omega_i} \tag{6}$$

$$V = kB_i v_i \omega_i \tag{7}$$

$$P_{out} = VI. \tag{8}$$

5. Conclusion

The effects of friction were neglected throughout the analysis, although these effects are by no means negligible and the analysis of the laboratory model was highly idealized.

In any case, real effects will further degrade performance and lead to greater pressure requirements — requirements that cannot be met by inlet dynamic head in a typical laboratory experiment. The implications of these results will be explored both theoretically and experimentally.

W. D. Jackson, R. J. Thome

B. LOSSES IN SUPERCONDUCTING Nb-$Zr_{25\%}$ SOLENOIDS AT LOW FREQUENCIES

For application of superconducting windings in an AC magnetic field system, the losses in such a system would have to be small enough to make them more attractive than the conventional windings. Losses in two small superconducting Nb-$Zr_{25\%}$ solenoids have been measured at low frequencies by using a calorimeter technique.

A complete description of the experimental apparatus and procedure has been given elsewhere.[1] Briefly, the test solenoid was placed inside an inverted bell jar, which was immersed in liquid helium. A long thin tube was attached to the top of the bell jar. The other end of the tube was connected to a flowmeter by means of a heat exchanger. The flowmeter was calibrated to read directly in milliwatts by dissipating a known amount of power inside the bell jar and measuring the corresponding rate of evaporation of helium. Excitation was provided by driving a known current through the solenoid.

The results for a 22-mH solenoid are shown in Figs. IX-2, IX-3, and IX-4. This solenoid was 1.25 inches long, and had a 9/16 inch bore. It was wound with 1457 turns of Nylon-coated Nb-$Zr_{25\%}$ wire of 0.015-inch diameter.

The frequency dependence of power loss is shown in Fig. IX-2. The loss is proportional to the 0.6 power of the frequency. This result does not agree with that obtained by Buchhold and Molenda,[2] or by Wisseman, Boatner, and Low.[3] They observed that for short straight sections of superconducting specimen, the loss had a linear frequency dependence.

Figure IX-3 shows the frequency dependence of excitation current for constant dissipation in the solenoid. It can be seen that, within experimental error, quantity $(I^4F)^n$ is constant. Extrapolation of characteristics shown in Fig. IX-2 shows that the loss p is proportional to I^2. Hence

$$P \propto I^2 F^{1/2}.$$

This is the same relationship that exists in normal conductors when skin effect is present. This relationship also implies that the effective resistivity ρ of the superconducting specimen is independent of current. This result agrees with that obtained by Zar,[4] who also observed that ρ is independent of current.

Figure IX-4 shows the variation of resistivity with frequency. The resistivity was found to be proportional to $F^{0.6}$ within the range of the parameters of the experiment.

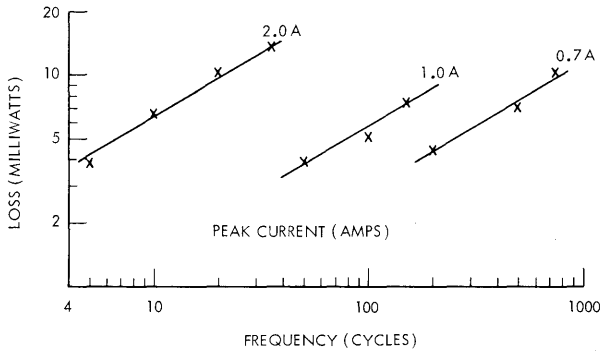

Fig. IX-2. Frequency dependence of power loss.

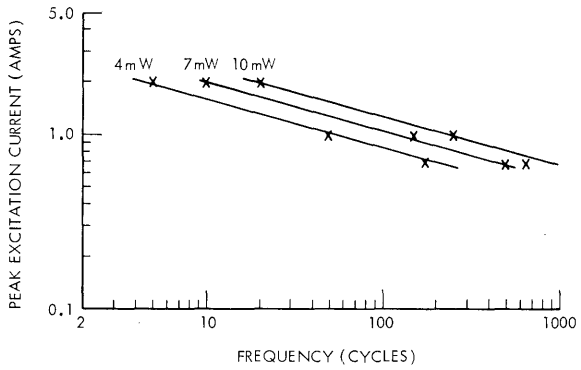

Fig. IX-3. Constant power characteristics.

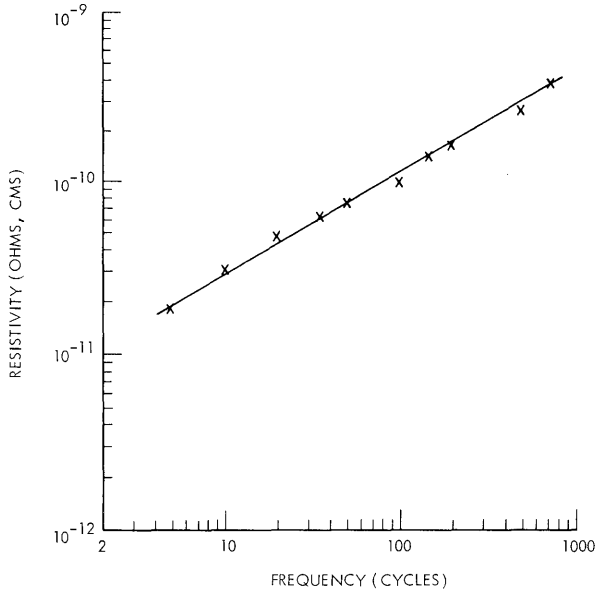

Fig. IX-4. Variation of resistivity with frequency.

This curve has the same characteristics above 500 cps as those obtained by Zar. There is reasonable quantitative agreement between the results of the Zar experiments and the present experiment above 100 cps.

These results do not agree with the results of Wisseman, Boatner, and Low, and of Buchhold and Molenda. In the present experiments and in those of Zar the specimens were solenoidal. It appears, therefore, that the different geometrical shape of the specimen was at least partly responsible for the divergent results.

Frequency dependence of critical current of the solenoid is shown in Fig. IX-5. It can be seen that below 10 cps, degradation in the current-carrying capacity of the solenoid increases faster than the heat dissipation. This indicates that in this region the solenoid was quenching because of bulk heating effects. The solenoid is obviously not quenching because of magnetic field effects. A probable reason appears to be mechanical resonance in the solenoid, which causes localized quenching.

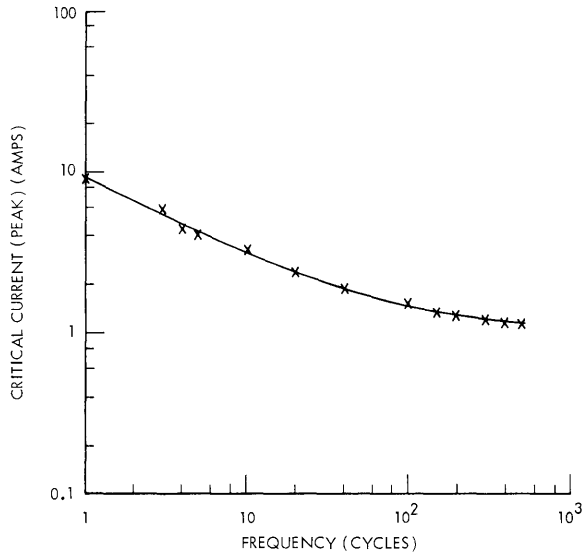

Fig. IX-5. Frequency dependence of critical current.

Mechanical vibrations are probably also responsible for the large disagreement in results for solenoidal specimens and straight-section specimens. Any dissipation in maintaining steady-state vibrations will be observed as a loss in the specimen. This loss will be in addition to that produced by localized quenching. In the case of a straight-section specimen, which generates its own magnetic field,[3] these vibrations will have little effect; hence, the observed losses will be lower. Similar results were also obtained for a 45-mH solenoid.

Losses in a superconducting winding system have been compared with those in a

nonsuperconducting optimally cooled system and a conventionally cooled system. These preliminary calculations indicate that an AC magnetic field system having liquid-hydrogen cooled copper winding (optimum operating temperature for copper is 21.2°K) would require only about half the power of an equivalent conventionally cooled system. In the calculations it is assumed that the refrigeration plant consumes approximately three times the power required by an ideal Carnot engine.

The superconducting winding system, at 100 cps, would require only 1/30-1/40 of the power consumed by a conventional winding. Five times the power requirements of a Carnot engine have been allowed for the refrigeration plant. At lower frequencies even larger savings should result. More experimental work with larger solenoids would be required to confirm this.

W. D. Jackson, A. N. Chandra

References

1. A. N. Chandra, Superconducting Solenoids under A.C. Excitation, S.M. Thesis, Department of Electrical Engineering, M.I.T., September 1964.

2. T. A. Buchhold and P. J. Molenda, Surface electrical losses of superconductors in low-frequency fields, Cryogenics 2, 344 (1962).

3. W. R. Wisseman, L. A. Boatner, and F. J. Low (Private communication, 1964).

4. J. L. Zar, Measurement of low resistance and the A.C. resistance of superconductors, Rev. Sci. Instr. 34, 801 (1963).

C. MAGNETOHYDRODYNAMIC INDUCTION MACHINE OF FINITE LENGTH

An MHD induction machine of infinite length has been considered previously.[1,2] For a machine that is not long compared with the entry length of the fluid into the traveling-field structure, there are severe discrepancies between performance calculations based on infinite and finite-length models. The solution has been obtained for a finite-length machine with an ideal iron core of infinite length, and with a lossless core of arbitrary permeability and infinite length.

1. Model

The model to be analyzed is shown in Fig. IX-6. The fluid flows in the x-direction between two parallel exciting plates of length ℓ and infinite extent in the z-direction, a distance 2a apart. The fluid velocity is assumed to be constant and in the x-direction to uncouple the electromagnetic and fluid equations and thus allow an analytical solution to be obtained. (This is not necessary for a slit-channel machine, $ak \ll 1$, because the field solution is independent of the velocity profile.[3] The slit-channel machine is the only case of practical interest.[4]) The region outside the plates is filled with a core of permeability μ_c and conductivity σ_c. The exciting plates, separated from the fluid and core by

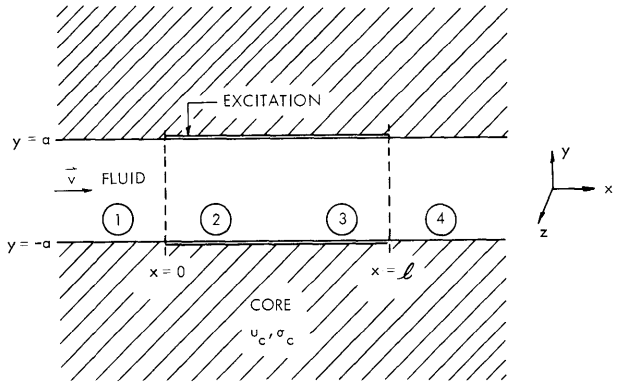

Fig. IX-6. The model.

insulators of infinitesimal thickness to prevent current flow in the y-direction, are assumed thin so that they can be replaced by current sheets with a surface conductivity $\sigma_s = \sigma_e b$, where b is the plate thickness, and σ_e the material conductivity. The plates are driven by a current source that gives a symmetric surface current density

$$\vec{K} = \vec{i}_z NI \cos(\omega t - kx), \tag{1}$$

which represents a traveling current wave of amplitude NI, frequency ω, wavelength $\lambda = 2\pi/k$, and velocity $v_s = \omega/k$. This is considered to be produced by a balanced two-phase system with sinusoidally distributed windings of maximum turns density N and peak current I. Only two-phase excitation is considered because an n-phase system can be reduced to a two-phase equivalent.

2. Transformed Potentials

The electromagnetic fields are determined from Maxwell's equations with the usual MHD approximation of neglecting displacement currents. Assuming constant velocity eliminates the need for the fluid equations. The analysis is simplified by the use of a vector potential $\vec{A}$ and scalar potential ϕ defined by

$$\vec{B} = \nabla \times \vec{A} \tag{2}$$

and

$$\vec{E} = -\nabla\phi - \frac{\partial \vec{A}}{\partial t}. \tag{3}$$

Noting that Ohm's law in a moving fluid is $\vec{J} = \sigma(\vec{E} + \vec{v} \times \vec{B})$, and substituting Eqs. 2 and 3 in Maxwell's equations gives

$$\nabla^2 \vec{A} - \mu\sigma \frac{\partial \vec{A}}{\partial t} + \mu\sigma(\vec{v} \times \nabla \times \vec{A}) = 0, \tag{4}$$

and

$$\nabla^2\phi - \mu\sigma \frac{\partial\phi}{\partial t} = 0. \tag{5}$$

Here,

$$\nabla \cdot \vec{A} + \mu\sigma\phi = 0 \tag{6}$$

has been chosen to uncouple Eqs. 4 and 5. The vector potential is in the z-direction and independent of z, and must have the same $e^{j\omega t}$ dependence as the exciting current, but the e^{-jkx} dependence of the excitation is preserved only in the driven part of the solution. Spatial transients, determined by the natural behavior of the system, exist because of the finite length. The analysis is simplified by writing the vector potential in complex notation

$$\vec{A}(x, y, t) = \mathrm{Re}\left\{\vec{i}_z \underline{A}(x, y)\, e^{j\omega t}\right\}. \tag{7}$$

The normal method of solving boundary-value problems is to determine the natural modes in each region from the geometry, and then use the boundary conditions to find the constants. The modes are not evident here, except for the special case of the ideal core considered below. Instead, the double-ended Laplace transform of the x-variation is taken. The transform used here is

$$\underline{A}(p, y) = \int_{-\infty}^{\infty} \underline{A}(x, y)\, e^{-pkx}\, dx, \tag{8}$$

where p is the complex transform variable, normalized with respect to the wave number k of the excitation. The transformed vector potentials are obtained from the transform of Eq. 4 for the fluid and core, by using the boundary conditions on the magnetic field at the fluid-core interface. The solution is

$$\underline{A_f}(p, y) = \frac{\mu_f \underline{K}(p) \cosh \gamma(p)\, ky}{k[\gamma(p) \sinh \gamma(p)a + \kappa\delta(p) \cosh \gamma(p)a]}, \quad |y| \leq a; \tag{9}$$

and

$$\underline{A_c}(p, y) = \frac{\mu_f \underline{K}(p)\, e^{-\delta(p)k(|y|-a)}}{k[\gamma(p) \tanh \gamma(p)a + \kappa\delta(p)]}, \quad |y| \geq a; \tag{10}$$

where

$$\gamma^2(p) = -p^2 + jR_M + R_M(1-s)\, p, \tag{11}$$

$$\delta^2(p) = -p^2 + jR_{Mc}, \tag{12}$$

$$s = \frac{v_s - v}{v_s}, \tag{13}$$

$$\kappa = \frac{\mu_f}{\mu_c}, \tag{14}$$

$$R_M = \frac{\mu_f \sigma_f v_s}{k}, \tag{15}$$

$$R_{Mc} = \frac{\mu_c \sigma_c v_s}{k}, \tag{16}$$

and $\underline{K}(p)$ is the transformed exciting current. The subscripts f, c, and e are used to denote fluid, core, and exciting-plate quantities, respectively; s is the slip in terms of synchronous speed v_s; and R_M and R_{Mc} are the fluid and core magnetic Reynolds numbers. These equations have the same form as for the infinite-length solution, but γ and δ are no longer constants.[1,2]

For a uniform traveling current of length ℓ,

$$\underline{K}(p) = \frac{NI\left[1 - e^{-(p+j)k\ell}\right]}{k(p+j)}. \tag{17}$$

This is just the sum of a positive step at $x = 0$ and a negative step at $x = \ell$, so that superposition can be used to find the total field solution. The field that is due to the negative step at the exit is the negative of the positive step solution, delayed in space by a length ℓ, and with the appropriate phase shift resulting from the negative step, $e^{-jk\ell}$.

The inverse transform for the vector potential is evaluated as a contour integral, which is the sum of the residues at the poles enclosed within the contour. The poles are the values of p at which the denominator is zero. One pole is evidently

$$p_e = -j, \tag{18}$$

which is due to the excitation; this gives the field with no ends. The other poles are determined by

$$\gamma \sinh \gamma a + \kappa\delta \cosh \gamma a = 0, \tag{19}$$

for which an analytical solution has been found only for an ideal iron core.[5,6]

3. Ideal Core – Fields and Impedance

For an ideal iron core, $\kappa = 0$, the natural poles occur when $\gamma = jn\pi$, or when

$$p_n^{\pm} = \frac{R_M(1-s)}{2}\left[1 \pm \sqrt{1 + \frac{j4}{R_M(1-s)^2} + \left(\frac{2n\pi}{aR_M(1-s)}\right)^2}\right]. \tag{20}$$

The ± sign of $p_n^{\pm}$ goes with the sign before the radical. The transform is not essential for this case, as the modes can be determined from the boundary conditions at the ideal iron core.

The residues at the poles are evaluated by expanding the denominator in a Taylor series about the pole. The case n = 0, treated separately because the series involves $\frac{0}{0}$, will differ in all equations by a factor of 2, so that it is convenient to define

$$\Delta_n = \begin{cases} 2 & n = 0 \\ 1 & n \neq 0. \end{cases} \tag{21}$$

The residues could also be obtained by using small-angle formulas.

Examination of the square-root term in Eq. 20 shows that the real part is always greater than one, and that both the real and imaginary parts are positive. The + poles, with positive real and imaginary parts, are the poles for negative x, since the natural response must decay away from the entrance. Similarly, the - poles have negative real and imaginary parts and apply to positive x. The vector potential that is due to the entrance is

$$\underline{A_f}(x,y) = -\sum_{n=0}^{\infty} \frac{\mu_f NI(-1)^n \cos\frac{n\pi y}{a}\, e^{p_n^+ kx}}{\alpha k \Delta_n \left(p_n^+ + j\right)\left(\frac{R_M(1-s)}{2} - p_n^+\right)} \qquad \text{for } x < 0, \tag{22}$$

and

$$\underline{A_f}(x,y) = \frac{\mu_f NI \cosh\gamma(-j)\, ky\, e^{-jkx}}{k\gamma(-j)\sinh\gamma(-j)\,\alpha} + \sum_{n=0}^{\infty} \frac{\mu_f NI\,(-1)^n \cos\frac{n\pi y}{a}\, e^{p_n^- kx}}{\alpha k \Delta_n \left(p_n^- + j\right)\left(\frac{R_M(1-s)}{2} - p_n^-\right)} \qquad \text{for } x > 0. \tag{23}$$

The inverse transform and the convergence condition for an infinite number of poles extending to infinity along the real axis are treated by Churchill.[7]

Further information about the field behavior is obtained by restricting attention to the regime of practical machine parameters; s ≪ 1 for high efficiency, $\alpha \ll 1$ for a reasonable power density, and $|sR_M| \gg 1$ for the reactive power to be small compared with the real power.[1] The value of $\alpha(1-s)R_M$ will probably be around unity, making the coefficient of n in the last term under the radical sign of Eq. 20 large and causing an appreciable increase in the poles from n = 0 to n = 1. The residues for n ≠ 0 are small compared with the residues for n = 0, and they decay much faster. The fields and powers, with a small error, can be calculated by using only the excitation and n = 0 components for this case. The powers resulting from the n ≠ 0 terms are at least two orders of magnitude

smaller than the powers that are due to the n = 0 components for reasonable parameter values.

Consider next the poles for n = 0. For the region of interest $\frac{4}{R_M(1-s)^2}$ will be less than one, and Eq. 20 may be written approximately

$$p_o^{\pm} = \frac{R_M(1-s)}{2}\left[1 \pm \left(1 + \frac{2j}{R_M(1-s)^2} + \frac{2}{R_M^2(1-s)^4}\right)\right], \tag{24}$$

with only the leading terms of the binomial series retained. The + pole has a decay length, $\frac{1}{2\pi\ \mathrm{Re}\left\{p_o^+\right\}}$ in wavelengths, of $\frac{1}{2\pi\ R_M(1-s)}$. This is small, a few hundredths of a wavelength. The - pole has a decay length of $\frac{R_M(1-s)^3}{2\pi}$, which is several wavelengths. This clearly shows that the perturbation fields may extend an appreciable distance into the machine.

The coil impedance for a finite-length machine, a function of the coil location, is

$$\frac{Z}{R_o} = \frac{1}{\mu_f v_s \sigma_s} + \frac{j}{\gamma(-j)\tanh \gamma(-j)\, a} + \sum_{n=0}^{\infty}\left\{\frac{j\left(e^{2\pi p_n^-} - 1\right)}{2\pi a \Delta_n \left(p_n^- + j\right)\left(\frac{R_M(1-s)}{2} - p_n^-\right)}\left[\frac{e^{\left(p_n^- + j\right)kx}}{\left(p_n^- + j\right)} \pm \frac{e^{\left(p_n^- - j\right)kx}}{\left(p_n^- - j\right)}\right]\right\} \tag{25}$$

for a coil one wavelength long. Here,

$$R_o = \frac{2\pi\mu_f v_s N^2 c}{k}. \tag{26}$$

The ± sign is for the two phases; + for the cos kx coils, and - for the sin kx coils. The first term is the resistance of the coil on account of its finite conductivity, the second is the impedance with no ends, and the remaining terms are the contribution from the perturbation field. The coil impedance is a function of x, where x is the location of the begining of the coil. For the cos kx coils, x is 0, λ, 2λ, etc. The exit fields are not included in this calculation, but their effect is small.

4. Ideal Core – Powers

The finite-length power calculations are considerably more complicated than for the infinite-length machine because of the infinite sums and the four distinct regions of space, as shown in Fig. IX-6. Regions 1 and 2 are before and after the entrance, and regions 3

and 4 are before and after the exit. For a long machine there is also a central core, where the infinite-machine condition exists. The field solution is already known in all space in terms of the entrance solution given above and the spatial and phase delays that are due to the negative step at the exit. The fields in regions 1 and 2 are the solutions obtained for $x < 0$ and $x > 0$ (Eqs. 22 and 23). The fields in regions 3 and 4 are the negative of those in regions 1 and 2, respectively, from the negative step, multiplied by $e^{-jk\ell}$ from the phase shift, and centered about $x = \ell$.

The power calculations are simplified by breaking up the powers by regions and sources, and by using the field properties. Only the power supplied by the exciting system to the fluid, P_s, and the mechanical power output, P_m, are considered, as the power dissipated in the fluid can then be determined. For convenience, the powers are split into four parts, determined by which field or fields are the sources; the excitation powers, the powers resulting from cross products between the excitation and perturbation fields, the perturbation powers attributable to fields at the entrance or exit alone, and the perturbation powers resulting from coupling between the entrance and exit fields. The powers are identified by numerical subscripts for the region, and by e for the excitation power and ep for the cross products. No subscript is used for the perturbation powers in P_m. The P_s terms are all e-p cross products, so no subscript is needed.

The results are listed in Table IX-2. There are no cross terms between the different values of n. There are P_m terms due to coupling between the entrance and exit fields, but no P_s terms. For a slit channel the only nonzero P_{mep} term is for $n = 0$, but this is the largest of all of the mechanical perturbation powers. Examination of the equations shows that P_{m1} is negative, P_{m4} is positive, and P_{s2} and P_{s3} reverse sign with the slip, s.

The results for the ideal-core powers are shown by the values of Table IX-3 for a machine that is 6 wavelengths long. The principal result is that the power output is decreased but the efficiency, $\frac{P_s}{P_m}$ for a generator, is only slightly changed. This is misleading; the total machine efficiency is decreased because, for the same viscous and excitation losses, less power output is obtained. The end effect is greater at small s and at small R_M. This limits the obtainable efficiency, and means that the smaller R_M machines obtained either with a plasma[1] or with a low-power output generator[4] are less efficient.

Oscilloscope pictures of the powers give further information about the dependence on machine length. In Fig. IX-7 only the set for $s = -0.2$, $R_M = 10$, and $\alpha = 0.1$ is shown because the general shape is the same for all curves. As s increases, the curves rise faster, while for small s or smaller R_M the slope decreases, as expected from Table IX-3. A very short machine operates as a flow damper, absorbing both electrical and mechanical input powers, so that some minimum length is required for generator operation.

Table IX-2. Powers for a machine of finite length.

Region 1

$$\frac{P_{m1}}{P_o} = -\frac{\alpha R_M(1-s)}{4\pi\ell}\,\mathrm{Re}\left\{\sum_{n=0}^{\infty}\frac{\Delta_n\left(j+(1-s)p_n^+\right)}{\left(p_n^+ + p_n^{+*}\right)}p_n^{+*}\,\underline{C_n^+}\,\underline{C_n^{+*}}\right\}$$

$$\frac{P_{s1}}{P_o} = 0$$

Region 2†

$$P_{m2} = P_{m2ep} + P_{m4}$$

$$\frac{P_{m2ep}}{P_o} = \frac{R_M(1-s)}{2\pi\ell}\,\mathrm{Re}\left\{\frac{jsp_o^{-*}\underline{C_o^{-*}}}{\gamma^2\left(p_o^{-*}-j\right)}\left(1-e^{\left(p_o^{-*}-j\right)2\pi\ell}\right)+\frac{j\left(j+(1-s)p_o^-\right)}{\gamma^{*2}\left(p_o^-+j\right)}\underline{C_o^-}\left(1-e^{\left(p_o^-+j\right)2\pi\ell}\right)\right\}$$

$$\frac{P_{s2}}{P_o} = -\frac{1}{2\pi\ell}\,\mathrm{Re}\left\{\sum_{n=0}^{\infty}\frac{j\left(1-e^{\left(p_n^-+j\right)2\pi\ell}\right)}{\Delta_n\alpha\left(p_n^-+j\right)^2\left(\frac{R_M(1-s)}{2}-p_n^-\right)}\right\}$$

Region 3†

$$P_{m3} = P_{m3ep} + P_{m1}$$

$$\frac{P_{m3ep}}{P_o} = \frac{R_M(1-s)}{2\pi\ell}\,\mathrm{Re}\left\{\frac{jsp_o^{+*}\underline{C_o^{+*}}}{\gamma^2\left(p_o^{+*}-j\right)}\left(1-e^{-\left(p_o^{+*}-j\right)2\pi\ell}\right)e^{j2\pi\ell}\right.$$

$$\left.+\frac{j\left(j+(1-s)p_o^+\right)}{\gamma^{*2}\left(p_o^++j\right)}\underline{C_o^+}\left(1-e^{-\left(p_o^++j\right)2\pi\ell}\right)e^{-j2\pi\ell}\right\}$$

$$\frac{P_{s3}}{P_o} = \frac{1}{2\pi\ell}\,\mathrm{Re}\left\{\sum_{n=0}^{\infty}\frac{j\left(1-e^{-\left(p_n^++j\right)2\pi\ell}\right)e^{-j2\pi\ell}}{\Delta_n\alpha\left(p_n^++j\right)^2\left(\frac{R_M(1-s)}{2}-p_n^+\right)}\right\}$$

†Excitation powers must be added to Regions 2 and 3.

Table IX-2 (continued).

Region 4

$$\frac{P_{m4}}{P_o} = \frac{\alpha R_M(1-s)}{4\pi\ell}\,\mathrm{Re}\left\{\sum_{n=0}^{\infty}\frac{\Delta_n\left(j+(1-s)p_n^-\right)}{\left(p_n^-+p_n^{-*}\right)}p_n^{-*}\,\underline{C_n^-}\,\underline{C_n^{-*}}\right\}$$

$$P_{s4} = 0$$

Coupling between Entrance and Exit

$$\frac{P_{m13}}{P_o} = \frac{\alpha R_M(1-s)}{4\pi\ell}\,\mathrm{Re}\left\{\sum_{n=0}^{\infty}\frac{\Delta_n\left(j+(1-s)p_n^+\right)}{\left(p_n^++p_n^{+*}\right)}p_n^{+*}\,\underline{C_n^+}\,\underline{C_n^{+*}}\left(e^{\left(j-p_n^{+*}\right)2\pi\ell}+e^{-\left(j+p_n^+\right)2\pi\ell}\right)\right\}$$

$$\frac{P_{m23}}{P_o} = \frac{\alpha R_M(1-s)}{4\pi\ell}\,\mathrm{Re}\left\{\sum_{n=0}^{\infty}\left[\frac{\Delta_n\left(j+(1-s)p_n^-\right)}{\left(p_n^-+p_n^{+*}\right)}p_n^{+*}\,\underline{C_n^-}\,\underline{C_n^{+*}}\,e^{j2\pi\ell}\left(e^{p_n^-2\pi\ell}-e^{-p_n^{+*}2\pi\ell}\right)\right.\right.$$

$$\left.\left.+\frac{\Delta_n\left(j+(1-s)p_n^+\right)}{\left(p_n^++p_n^{-*}\right)}p_n^{-*}\,\underline{C_n^+}\,\underline{C_n^{-*}}\,e^{-j2\pi\ell}\left(e^{p_n^{-*}2\pi\ell}-e^{-p_n^+2\pi\ell}\right)\right]\right\}$$

$$\frac{P_{m24}}{P_o} = \frac{-\alpha R_M(1-s)}{4\pi\ell}\,\mathrm{Re}\left\{\sum_{n=0}^{\infty}\frac{\Delta_n\left(j+(1-s)p_n^-\right)}{\left(p_n^-+p_n^{-*}\right)}p_n^{-*}\,\underline{C_n^-}\,\underline{C_n^{-*}}\left(e^{\left(p_n^-+j\right)2\pi\ell}+e^{\left(p_n^{-*}-j\right)2\pi\ell}\right)\right\}$$

Totals

$$P_m = P_{me} + P_{m2ep} + P_{m3ep} + 2P_{m1} + 2P_{m2} + P_{m13} + P_{m23} + P_{m24}$$

$$P_s = P_{se} + P_{s2} + P_{s3}$$

Normalization

$$P_o = \frac{\mu_f v_s N^2 I^2 c 2\pi\ell}{k}, \qquad \ell \text{ in wavelengths}$$

$$\underline{C_n^{\pm}} = \mp\frac{(-1)^n}{\Delta_n\alpha\left(p_n^{\pm}+j\right)\left(\frac{R_M(1-s)}{2}-p_n^{\pm}\right)}$$

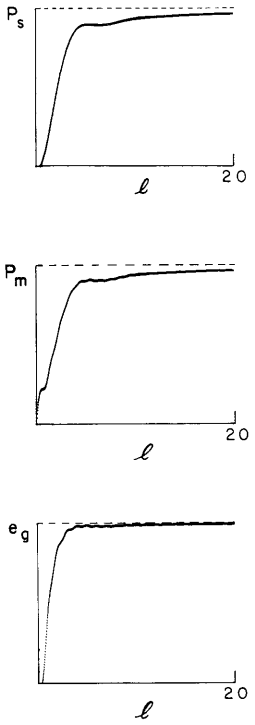

Fig. IX-7. P_s, P_m, and efficiency for a finite-length machine vs length ℓ. (s = -0.2, R_M = 10, a = 0.1, and total range of ℓ is 20 wavelengths.)

Table IX-3. Total powers and efficiencies for a machine that is six wavelengths long.

s	R_M	a	P_s^*	P_M^*	e(%)	$e_\infty^\dagger$(%)
-0.05	10	0.1	0.483	0.537	85.6	95.2
-0.1	10	0.1	0.697	0.723	87.6	90.0
-0.2	10	0.1	0.897	0.909	82.3	83.3
-0.3	10	0.1	0.927	0.939	75.9	76.9
-0.5	10	0.1	1.008	1.002	67.0	66.7
-1	10	0.1	0.997	0.997	50.0	50.0
-0.01	100	0.1	0.033	0.049	66.6	99.0
-0.1	100	0.1	0.971	0.971	90.9	90.9
-0.2	5	0.1	0.842	0.866	81.0	83.3
-0.2	1	0.1	0.716	0.841	71.0	83.3

*P_s, P_m are normalized to be 1 if there is no end effect.

†e_∞ is the efficiency with no end effect, $\frac{1}{1-s}$.

5. Lossless-Core Machine

A machine with a lossless core of arbitrary permeability is treated by an extension of the previous theory. The arbitrary core problem is more complicated for the following reasons.

1. An analytical solution for the poles is not available, although equations can be found for the fields and powers in terms of the unknown poles.
2. The fields are no longer orthogonal for the power calculations.
3. The fields are not zero in the core.

The solution is described, but not carried through in the same detail as for the ideal-core machine.

The poles for a lossless core, $\delta = 1$, are determined from Eq. 19. Writing γ as the sum of real and imaginary parts shows that γ must be pure imaginary, $\gamma = jb$, and that

$$b \tan ba - \kappa = 0. \tag{27}$$

The roots of Eq. 27, denoted by b_n, cannot be determined analytically, although numerical methods are available. For $\kappa a \ll 1$ or $ba \gg 1$, the roots become the same as for the ideal core.

The poles, in terms of these roots, are

$$p_n^{\pm} = \frac{R_M(1-s)}{2}\left[1 \pm \sqrt{1 + \frac{j4}{R_M(1-s)^2} + \left(\frac{2b_n}{R_M(1-s)}\right)^2}\right]. \tag{28}$$

The poles for an arbitrary core lie at different points on the same curve in the p-plane as the ideal-core poles.

There is one important distinction for the nonideal core. The lowest root, b_o, is no longer zero, but lies between zero and $\pi/2a$. The real part of the square root of Eq. 28 for $n = 0$ will be larger, and the decay length for p_o^- significantly less than for an ideal core. For the practical parameter values $s = -0.1$, $R_M = 10$, and $a = 0.1$, the decay length is 2.1 wavelengths for an ideal core, but only 0.19 wavelength for an air core. The other roots, and thus the poles, are essentially unchanged. The zero-order field will not be much larger than the others and will not dominate the powers. The perturbation field decays faster, and for this reason may have a smaller net effect on the performance.

The vector potential is

$$\underline{A_f}(x,y) = -\sum_{n=0}^{\infty} \frac{\mu_f N I b_n^2 \cos b_n ky\, e^{p_n^+ kx}}{k(\cos b_n a)\left[\kappa + a\left(\kappa^2 + b_n^2\right)\right]\left[\frac{R_M(1-s)}{2} - p_n^+\right]\left(p_n^+ + j\right)} \quad \text{for } x < 0 \tag{29}$$

and

$$\underline{A_f}(x,y) = \frac{\mu_f NI \cosh \gamma k y \, e^{-jkx}}{k(\gamma \sinh \gamma a + \kappa \cosh \gamma a)}$$

$$+ \sum_{n=0}^{\infty} \frac{\mu_f NI b_n^2 \cos b_n k y \, e^{\bar{p}_n kx}}{k(\cos b_n a)\left[\kappa + a\left(\kappa^2 + b_n^2\right)\right]\left[\frac{R_M(1-s)}{2} - \bar{p}_n\right]\left(\bar{p}_n + j\right)}, \qquad \text{for } x > 0. \tag{30}$$

The impedance for a coil that is 1 wavelength long, calculated as before, is

$$\frac{Z}{R_o} = \frac{1}{\mu_f v_s \sigma_s} + \frac{j}{\gamma \tanh \gamma a + \kappa}$$

$$+ \sum_{n=0}^{\infty} \frac{j b_n^2 \left(e^{2\pi \bar{p}_n} - 1\right)\left[\frac{e^{\left(\bar{p}_n + j\right)kx}}{\left(\bar{p}_n + j\right)} \pm \frac{e^{\left(\bar{p}_n - j\right)kx}}{\left(\bar{p}_n - j\right)}\right]}{2\pi\left[\kappa + a\left(\kappa^2 + b_n^2\right)\right]\left[\frac{R_M(1-s)}{2} - \bar{p}_n\right]\left(\bar{p}_n + j\right)}, \tag{31}$$

in which the terms are the same as those described for the ideal core. The arbitrary core powers are much more complicated because many of the terms that dropped out for an ideal core have to be retained now.

E. S. Pierson, W. D. Jackson

References

1. W. D. Jackson, E. S. Pierson, and R. P. Porter, Design Considerations for MHD Induction Generators, International Symposium on Magnetohydrodynamic Electrical Power Generation, Paris, July 6-11, 1964.

2. E. S. Pierson, Power flow in the magnetohydrodynamic induction machine, Quarterly Progress Report No. 68, Research Laboratory of Electronics, M. I. T., January 15, 1963, pp. 113-119.

3. E. S. Pierson, The MHD Induction Machine, Sc. D. Thesis, Department of Electrical Engineering, M. I. T., Cambridge, Massachusetts, 1964, Section 4. 3.

4. Ibid., Chapter 7.

5. J. B. Fanucci, et al., Electrodeless MHD Generator Research, Part I: Theoretical Analysis, ASD-TDR-62-411, Part I, Radio Corporation of America, Moorestown, New Jersey, October 1962.

6. R. N. Sudan, Interaction of a conducting fluid stream with a traveling wave of magnetic field of finite extension, J. Appl. Phys. 34, 641-650 (1963).

7. R. V. Churchill, Operational Mathematics (McGraw-Hill Book Company, Inc., New York, 2d edition, 1958), pp. 201-206.

D. PENETRATION COEFFICIENT FOR AN ION IN A PARTIALLY MOBILE FILM

1. Introduction

The importance of an adsorbed monolayer of cesium on the electrode surfaces in thermionic converters has been treated in great detail.[1,2] The relation between changes in electron work function and ionic heat of adsorption has been expressed by the penetration coefficient $f = \Delta\phi_i/\Delta\phi_e$. This relation has been theoretically obtained for two limiting types of adsorbed films, perfectly mobile and perfectly immobile.[3] These theoretical expressions have been useful in interpretations of the effects of cesium fluoride additives on collector surfaces.[4]

Since the actual adsorbed film is neither perfectly mobile nor perfectly immobile, experimental values for f fall between the two limiting cases, approaching the penetration coefficient obtained for perfectly immobile film as the coverage increases. This is to be expected because at low coverages the thermal effects are comparable to the particle interaction, and thus the particles in the adsorbed layer have enough thermal energy to become partially mobile. These thermal effects have been accounted for previously[5] in an approximate manner. In this report, thermal effects are considered from an exact, statistical mechanical point of view, thereby enabling derivation of the penetration coefficient for a partially mobile film, which agrees well with experimental data[6] over the entire range of coverage.

2. Theory

The immobile film has been defined as that film which displays a well-ordered array of adsorbates in which all adsorbates are equally spaced from each other. This model has been described in detail previously.[3]

The results of the previous analysis may be summarized as follows.

(i) Potential of an ion in an immobile film,

$$V_{im} = \frac{2.25q\lambda^2}{d^3}\theta_i^{1/2}.$$

(ii) Potential at infinity relative to the surface,

$$V_\infty = 2\pi M\sigma_1\theta_i = \frac{\pi q\lambda\theta_i}{d^2}.$$

(iii) Penetration coefficient for immobile film,

$$f_{im} = 1 - \frac{V_{im}}{V_\infty} = 1 - \frac{2.25\lambda}{\pi d}\theta_i^{1/2}.$$

As the equilibrium temperature of the monolayer is raised above T = 0°, thermal energy will displace some of the ions from the well-ordered array of the immobile film. Since an ion can be at any potential between V_{im} and ∞, there exists an effective potential at any θ above that given by (i). This effective potential increase is given by

$$\Delta V = \frac{1}{N}\int_{V_{im}}^{\infty} V\, e^{-\frac{V}{kT}}\, dg, \tag{1}$$

where dg = density of states as a function of V. If the adsorbate density on the surface is uniform and given by $\rho = \theta_i/4d^2$, then the density of states is written

$$dg = \rho\, dA = \left(\frac{\theta_i}{4d^2}\right) dA = \left(\theta_i \frac{\pi}{2d^2}\right) r_{ij}\, dr_{ij}, \tag{2}$$

with r_{ij} as identified in the previous report.[3] It has been shown that r_{ij} is expressible in terms of V as

$$V = \frac{2q\lambda^2}{r_{ij}^3}. \tag{3}$$

Equation 3 solved for r_{ij} and placed in Eq. 2 yields

$$dg = \left(\theta_i \frac{\pi}{6d^2}\right)(2q\lambda^2)^{2/3}\, V^{-5/3}\, dV. \tag{4}$$

Let $u(\theta) \equiv V(\theta)/kT$. Use of this transformation and of Eq. 4 in Eq. 1 yields

$$\Delta V = \left(\theta_i \frac{\pi}{6d^2}\right)(2q\lambda^2)^{2/3}(kT)^{1/3}\int_{u_{im}}^{\infty} e^{-u}\, u^{-2/3}\, du \tag{5}$$

for the single adsorbate.

The penetration coefficient for the partially mobile film is given by

$$f = 1 - \frac{V_{im} + \Delta V}{V_\infty} = f_{im} - \frac{\Delta V}{V_\infty}. \tag{6}$$

Using result (ii) above and Eqs. 5 and 6 for cesium adsorbed on tungsten (λ = 1.65 Å, d = 3.15 Å), we obtain

$$f = f_{im} - 0.056\left(\frac{T}{1000}\right)^{1/3}\int_{u_{im(\theta)}}^{\infty} e^{-u}\, u^{-2/3}\, du. \tag{7}$$

The integral is an incomplete gamma function that has been evaluated by Koskinen[7] in the following manner. Let $u = w^3$ so that Eq. 7 becomes

$$f = f_{im} - 0.168 \left(\frac{T}{1000}\right)^{1/3} \left[\int_0^{\infty} e^{-w^3}\, dw - \int_0^{w_{im}=u^{1/3}} e^{-w^3}\, dw\right] \tag{8}$$

which, with T = 800°K (the mean value of temperature for Taylor-Langmuir data), becomes

$$f = f_{im} - 0.14 + 0.156 \int_0^{w_{im}(\theta)} e^{-w^3}\, dw. \tag{9}$$

This is the form of the integral that has been evaluated by Koskinen[7] as a function of the upper limit. By using these results and those of the previous report[3] for f_{im}, the curve

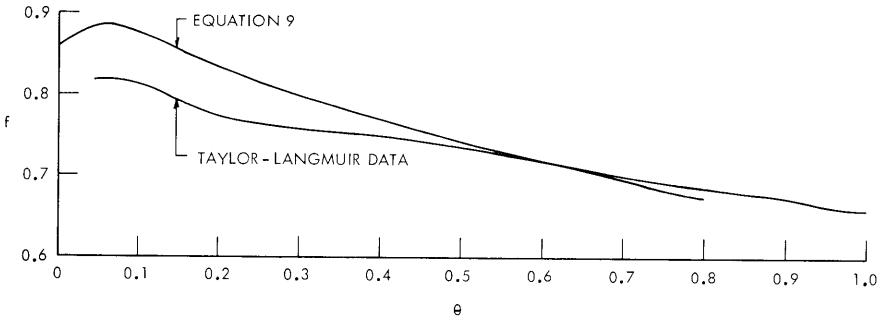

Fig. IX-8. Penetration coefficient for partially mobile film vs coverage.

of Eq. 9 can be drawn against coverage as in Fig. IX-8. Also shown there are the experimental values obtained from Taylor-Langmuir data.

3. Conclusions

Experimental values for the penetration coefficient are in excellent agreement with theoretical values of Eq. 9 for a partially mobile film. Therefore it may be concluded that the adsorbed film is accurately described as a partially mobile film. As is to be expected, as the coverage increases, particle interactions increase and thus the film can be described as an immobile film; but, at low coverage, temperature dependence must be included in order to obtain valid results. Accurate values for the penetration coefficient have been obtained through a theoretical formulation that is valid for the entire range of coverage.

J. W. Gadzuk

References

1. E. N. Carabateas, Analytical Description of Cesium Films on Metals, Report to the National Science Foundation, "Basic Studies of Cesium Thermionic Converters," June 1964.

2. N. S. Rasor and C. Warner III, Correlation of emission processes for adsorbed films, J. Appl. Phys. 35, 2589 (1964).

3. J. W. Gadzuk, Penetration of an ion through an ionic dipole layer at an electrode surface, Quarterly Progress Report No. 72, Research Laboratory of Electronics, M. I. T., January 15, 1964, pp. 166-174.

4. E. N. Carabateas, Displacement of the Collector Work-Function Minimum in the Temperature Ratio Plot, Report on the Twenty-fourth Annual Conference on Physical Electronics, Massachusetts Institute of Technology, March 25-27, 1964, pp. 185-195.

5. J. W. Gadzuk, The Penetration of an Ionic Dipole Layer at an Electrode Surface, Report on the Twenty-fourth Annual Conference on Physical Electronics, op. cit., pp. 50-56.

6. J. B. Taylor and I. Langmuir, Phys. Rev. 44, 423 (1933).

7. M. F. Koskinen, Personal communication, July 1964.

E. ELECTRON AND ION EMISSION FROM A TUNGSTEN MONOCRYSTAL

1. Introduction

The work functions of the different crystallographic orientations of a single-crystal tungsten filament in vacuo have been obtained and the results compare well with data obtained by Nichols,[1] Smith,[2] and Hutson.[3] The vacuum measurements, including collector bias (with respect to the emitter) data, anode bias data, guard-ring bias (with respect to the collector) data, Richardson data, and an emission map of the different crystallographic faces, indicated that the tube would be a satisfactory test vehicle for taking emission measurements in cesium vapor.

2. Description of the Apparatus

A schematic diagram of the tube and associated circuitry used to take cesium measurements is shown in Fig. IX-9. The tungsten crystal is a 0.003-inch diameter wire in the center of the tube. It is enclosed by a concentric cylindrical tantalum anode, which is enclosed by a cylindrical collector with guard rings on both sides. The guard rings and collector are of platinum which has been painted on the glass walls. A slit in the anode subtends an angle of 4.0° on the filament. Two iron slugs encased in glass are spot-welded to the anode so that it can be rotated from outside the tube by magnets. To measure electron emission, the anode was typically biased at 1 kilovolt positive with respect to the filament, and the collector at 6 volts positive. The entire tube was placed in an oil bath regulated within 0.1°C in temperature.

3. Experimental Techniques

After the cesium ampule was broken, preliminary attempts to obtain collector bias curves and "S" curves indicated that the two major barriers to taking reliable data were leakage currents across the glass walls of the tube and contamination in the tube.

Even though the tube had been well outgassed and pumped down to a pressure of a

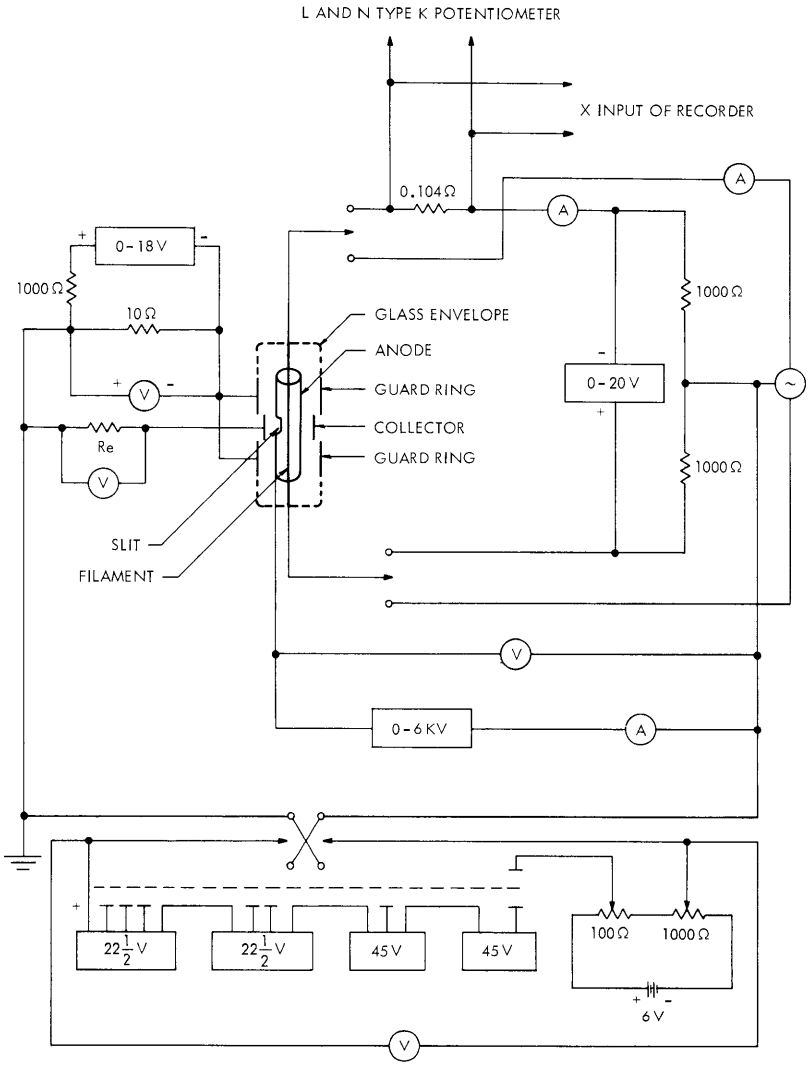

Fig. IX-9. Schematic diagram of the tube and circuit used for cesium measurements.

few times 10^{-11} torr before breaking the cesium ampule, the decay of electron emission currents to approximately half of their original values, 30 minutes after flashing the filament to a high temperature, indicated that some type of contaminate was present in the tube. Best[4] has shown that large quantities of hydrogen are evolved when Pyrex is exposed to alkali metals. Thus, some degradation of emission, which is due to hydrogen, was expected. The results of Stickney[5] indicate, however, that the addition of H_2 to a Cs-W system actually enhances the emission. Therefore there is some doubt about the nature of the contamination. Flashing the titanium getter on the tube only marginally decreased the amount of contamination. The technique used to avoid the decay of

emission was to flash the tungsten crystal at approximately 2050 °K (or above) and plot the "S" curve on an X-Y recorder as the crystal was cooled to the bath temperature. An "S" curve could be taken in a couple of minutes in this manner, in contrast to the hour (or more) required in the more tedious point-by-point method.

We found that the resistance of each of the guard rings from one end to the other was too great to effectively shield the collector from leakage currents when the guard rings were simply grounded. The resistance of the heated folds between the guard rings and the collector was of the order of 10^5 ohms when the folds were at approximately 150°C. This resistance was somewhat less than expected. The combination of high-resistance guard rings and low-resistance leakage paths produced leakage currents of the order of 10^{-7} amp (or more) at typical anode and collector bias values. These leakage currents to the collector are larger than the emission currents to the collector. We found, however, that the leakage currents could be balanced out by biasing the guard ring at approximately 3 millivolts negative with respect to ground. This balance was apparently not affected by the voltage applied across the filament to heat it. By using this "bucking voltage," the leakage currents were reduced to less than 1×10^{-9} amp (3.8×10^{-4} amp/cm^2), and the following results could be obtained.

4. Results

An "S" curve of electron emission from the (110) face at a cesium temperature of 40°C is shown in Fig. IX-10. This curve was found to be quite reproducible and to be independent of the electrometer input resistance R_E, as long as R_E was no greater than 10^3 ohms. At $R_E = 10^4$ ohms, the collector current decreased approximately 25 per cent; this is consistent with the value, $\sim 10^5$ ohms, for the leakage resistance between the guard rings and collector.

The data appeared to be qualitatively the same as data taken on polycrystalline surfaces by other workers.[6,7] The actual values of the observed currents were an order of magnitude larger than those observed by Taylor and Langmuir.[6] This is surprising, since they assumed that their polycrystalline surface was composed primarily of (110) faces. The effective work function at the low-temperature peak (T=750°K) of the "S" curve is 1.62 ev at zero field. The minimum work function observed by Taylor and Langmuir was 1.70 ev.

At the high-temperature end of the curve, the last four points fall on a straight line with a Richardson slope ϕ_R of 2.34 ev at zero field. At these temperatures ($\geq$1900°K), the surface should be completely free of cesium and the measured currents should be identical to those measured in vacuo. The ϕ_R of 2.34 ev is, however, half that measured by Nichols[1] and by Smith.[2] At the low values of electron emission, there is apparently some distortion of the curve because of leakage currents.

There is no obvious explanation for these anomalously high values of electron

emission. Spurious effects, such as secondary electrons, x-ray electrons or photoelectrons produced at the collector and accelerated to the anode, would decrease the

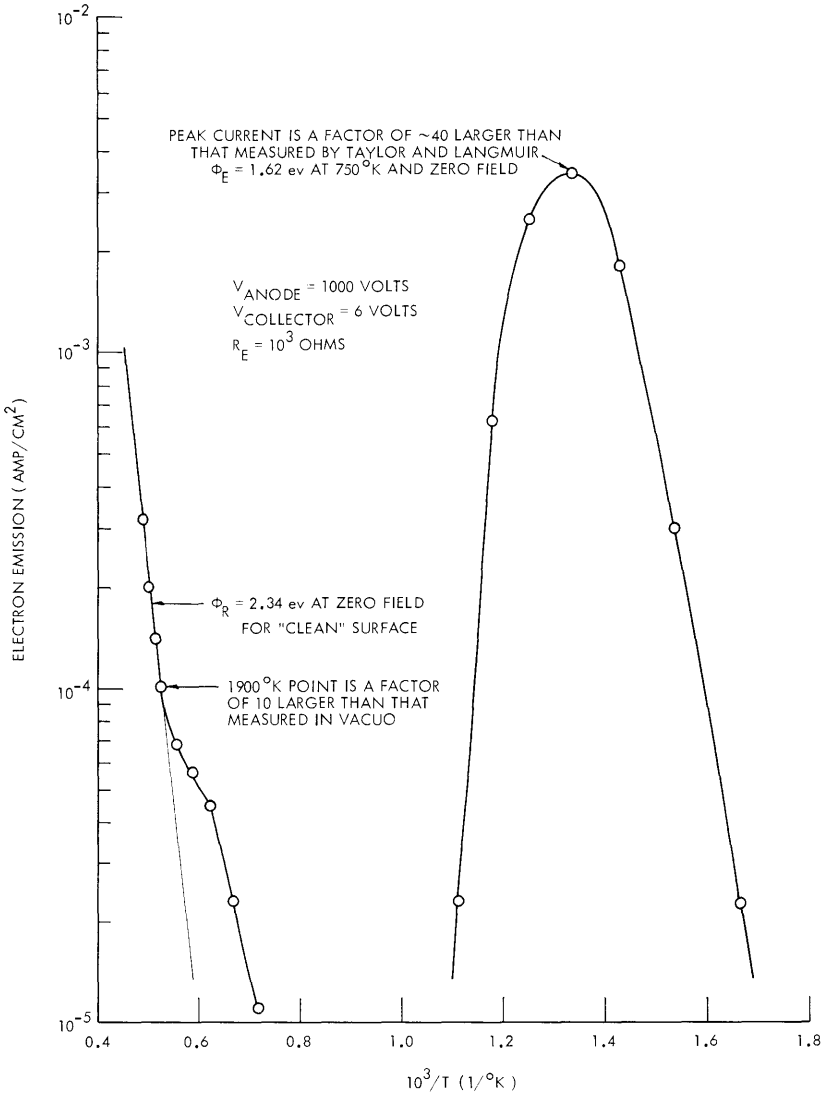

Fig. IX-10. "S" curve on (110) face at T_{Cs} = 40°C.

current measured at the collector. It is possible that the leakage currents were not completely balanced out by the bucking-voltage technique.

The tube developed a leak after these data were taken and, in an attempt to prepare the tube for reprocessing on the vacuum system, the platinum guard rings and collector were washed off the glass walls. Apparently the poor bond between the platinum and the glass was the major cause of the high resistance of the guard rings.

5. Summary and Future Plans

A new tube with a more elaborate guard-ring system is being constructed. The platinum guard rings and collector have been evaporated onto the glass, instead of painted on as before. It is hoped that these guard rings will eliminate the troublesome leakage currents and thus help determine whether the observed high values of collector current are due to spurious effects, or are actually electrons emitted from the surface under study. Measurements of ion currents should provide a cross-check on the measured values of work function.

J. L. Coggins

References

1. M. H. Nichols, Phys. Rev. 57, 297 (1940).

2. G. F. Smith, Phys. Rev. 94, 295 (1954).

3. A. R. Hutson, Phys. Rev. 98, 889 (1955).

4. W. V. Best, Ph. D. Dissertation (Physical Chemistry), University of Missouri, 1963.

5. R. E. Stickney, Report on the Twenty-Fourth Annual Conference on Physical Electronics, M. I. T., March 25-27, 1964, p. 243.

6. J. B. Taylor and I. Langmuir, Phys. Rev. 44, 423 (1933).

7. J. M. Houston, Bull. Am. Phys. Soc. II 6, 358 (1961).